



Fabrication and electrochemical performance of spinel copper manganese oxide nanocomposites for supercapacitor application

KANAGARAJAN KIRUTHIKA¹, VELAYUTHAM RENUGA^{1,*} 
and VEMBU SURYANARAYANAN²

¹PG and Research Department of Chemistry, National College (Autonomous), Tiruchirappalli 620001, India

²Electroorganic and Materials Electrochemistry Division, CSIR-Central Electrochemical Research Institute, Karaikudi 630003, India

*Author for correspondence (dr.v.renuga@gmail.com)

MS received 14 October 2022; accepted 10 January 2023

Abstract. In this study, the spinel copper manganese oxide (CMO) nanocrystals were synthesized by simple chemical co-precipitation method and was characterized by Fourier transform infrared spectroscopy, X-ray diffraction, X-ray photoelectron spectroscopy, scanning electron microscopy and transmission electron microscopy (TEM). The morphology of the material found from TEM is to be spherical in shape with the crystallite size of 3.51 nm. The electrochemical characterizations of the CMO were performed by cyclic voltammetry, galvanostatic charge/discharge and electrochemical impedance spectroscopy. The specific capacitance of CMO was found to be 280 F g⁻¹ at a current density of 1 A g⁻¹. To enhance its capacitance value, it was doped with multi-walled carbon nanotube and poly(3,4-ethylenedioxythiophene) polystyrene sulphonate (PEDOT:PSS) and their electrochemical characterizations were recorded and compared with CMO. Doped material (CMO/MWCNT/PEDOT:PSS) exhibits a high specific capacitance of 1087 F g⁻¹ at current density of 1 A g⁻¹ with a good rate performance and retained an excellent electrochemical stability of 104% capacitance retention and coulombic efficiency of 101% over 10,000 cycles at a current density of 5 A g⁻¹. This work recommends an idea for such advanced electrode material for efficient supercapacitors.

Keywords. Chemical co-precipitation; copper manganese oxide; MWCNT; PEDOT:PSS; supercapacitor.

1. Introduction

The requirement for energy storage devices is becoming high due to the depletion of our natural resources, increase in population and also high usage of electronic devices like mobile phones, laptops, etc. [1]. The energy storage devices like battery due to poor conductivity cannot attain high energy storage capacity. Though conventional capacitors provide high energy storage capacity, the energy and power densities are lower than batteries due to their low surface area. Hence, supercapacitors lead a role to bridge the gap between batteries and conventional capacitors. They are promising devices for energy storage applications as they exhibit high surface area and long cycle life resulting in higher energy density than capacitors and greater power density than batteries [2]. They are being considered for various applications as power sources for pulsed light generators, lasers, camera flash equipment and backup power source for computer memory [3, 4]. They are categorized into three types depending on the nature of electrode materials and mechanism involved for the storage of charge, namely electrical double-layer capacitor (EDLC), pseudocapacitor and hybrid capacitor. EDLC stores charge

electrostatically (non-Faradaically) and there is no transfer of charge between electrode and electrolyte [5]. For example, different forms of carbon materials like graphene [6] and CNT [7] can be used to store charge in EDLC electrodes. In pseudocapacitors, charge storage arises from the fast reversible surface faradic reactions happening at electrode/electrolyte interface. Metal oxides/hydroxides/sulphides [8–10] and conducting polymers like polyaniline [11], PEDOT:PSS [12], polypyrrole [13] are good examples of pseudocapacitors. In hybrid capacitor, the charge storage arises from the combination of both faradaic and non-faradaic processes and it has the ability to achieve longer cycle life, greater energy and power densities than EDLC [14]. In recent times, nanomaterial-based supercapacitors play a vital role in the energy storage applications [15]. Researchers are searching for the energy storage device which is eco-friendly, reusable, conversion efficiency and long cycle life with high energy density and great power density [16].

Due to high storage capacity and earth abundance, transition metal oxides (TMOs) with spinel-type nanomaterials have attracted the attention of researchers worldwide recently [17, 18]. Many TMOs with properties of

supercapacitors such as NiCo_2O_4 [19], MnCo_2O_4 [20], CuCo_2O_4 [21], CoFe_2O_4 [22], NiFe_2O_4 [23] and CuFe_2O_4 [24] have been reported. Among the TMOs, copper and manganese are abundant, eco-friendly and of low cost compared to other metals such as nickel and cobalt. Copper oxide [25] and manganese oxide [26] are among the most investigated metal oxides for supercapacitor applications. Though having large working potential window with low electrical conductivity [27], manganese oxide could not serve as a good electrode in supercapacitor. Moreover, the chemical instability of copper oxide [28] also limits its usage as an efficient electrode. Whereas, when manganese oxide combines with copper oxide as copper manganese oxide (CMO), it serves as capable electrode material. In recent times, many researchers concentrated on preparing CMO by different synthetic methods, such as hydrothermal [29], sol-gel [30], ceramic [31], co-precipitation [32, 33], micro-emulsion [34], novel combustion [35], mechanochemical [36], solid-state reaction [37] and thermal oxidation method [38].

Chen *et al* [39] designed a unique cupric oxide–manganese dioxide on a copper grid for high-performance supercapacitors with a very high specific capacitance of 343.9 F g^{-1} at a current density of 0.25 A/g along with a good rate capability. Similarly, Saravanakumar *et al* [40] reported CuMn_2O_4 electrode material prepared by solvothermal method with specific capacitance value of 571.6 F g^{-1} at 1 A g^{-1} [40]. Recently, Sheikhzadeh and Sanjabi [41] reported spinel CuMn_2O_4 electrode material prepared by electrodeposition method with the specific capacitance value of 744 F g^{-1} at 10 mV s^{-1} and the retention capacitance of 91% of 10,000 cycles. But Jingbin *et al* [42] reported $\text{Cu}_{1.5}\text{Mn}_{1.5}\text{O}_4$ spinel oxide as a novel anode material for lithium-ion batteries that retain a specific

capacity of 464 mAh g^{-1} at a current of 100 mA g after 60 cycles.

In view of all these reports, we aimed to synthesize copper manganese oxide, $\text{Cu}_{1.5}\text{Mn}_{1.5}\text{O}_4$ (CMO), spinel nanocrystal by simple chemical co-precipitation method. The CMO was characterized for its functional group by Fourier transform infrared spectroscopy (FTIR), phase structure by X-ray diffraction (XRD) analysis, whereas the morphology and particle size were analysed by recording their scanning electron microscopy (SEM) and transmission electron microscopy (TEM). Further its electrochemical properties like cyclic voltammetry (CV), galvanostatic charge/discharge (GCD) and electrochemical impedance spectroscopy (EIS) were studied. The specific capacitance of CMO was found to be 280 F g^{-1} at a current density of 1 A g^{-1} . Further to enhance its capacitance value, it was doped with a carbon material—multi-walled carbon nanotube (MWCNT), a conducting polymer—poly (3,4-ethylenedioxy thiophene) polystyrene sulphonate (PEDOT:PSS) separately and in a combination of MWCNT and PEDOT:PSS denoted as CMO/MWCNT/PEDOT:PSS and their electrochemical performance were recorded. By such doping, a high specific capacitance of 1087 F g^{-1} at a current density of 1 A g^{-1} was obtained bearing 104% capacitance retention with a coulombic efficiency of 101% over 10,000 cycles, and at a current density of 5 A g^{-1} was obtained for CMO/MWCNT/PEDOT:PSS.

2. Experimental

2.1 Materials

Copper acetate, manganese acetate, sodium hydroxide, 1-methyl-2-pyrrolidone (NMP) and ethanol (99.9%) were

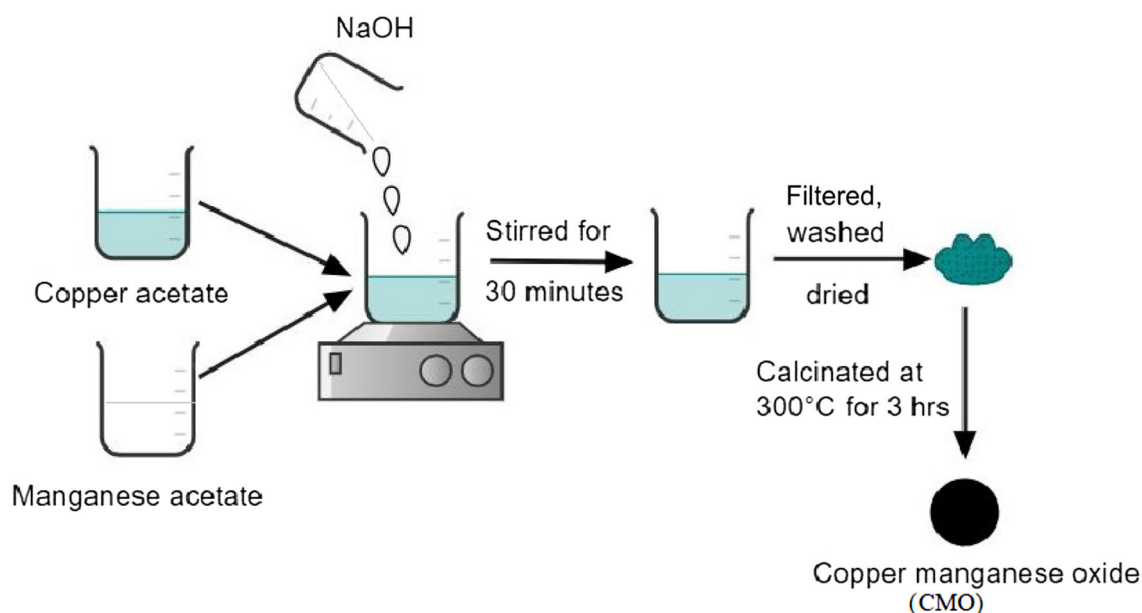


Figure 1. Schematic diagram for the synthesis of CMO.

Table 1. Percentage composition of different electrode materials.

Electrode	% of Active material			Mixing procedure
	CMO	MWCNT	PEDOT:PSS	
CMO	80	—	—	CMO was ground to powder
CMO/MWCNT	75	5	—	CMO was ball milled with MWCNT to obtain CMO–MWCNT composite
CMO/PEDOT:PSS	75	—	5	CMO was added to PEDOT:PSS and ultrasonicated for proper mixing to get CMO–PEDOT:PSS composite
CMO/MWCNT/PEDOT:PSS	75	2.5	2.5	CMO was ball milled with MWCNT then PEDOT:PSS is added and ultrasonicated to get CMO/MWCNT/PEDOT:PSS composite



Figure 2. Active material coated on nickel foam.

purchased from Merck specialities Private Limited, India. Multi-walled carbon nanotube (MWCNT) was purchased from Sisco Research Laboratory, India. Poly(3,4-ethylene-dioxythiophene) polystyrene sulphonate (PEDOT:PSS), polyvinylidene difluoride (PVDF), acetylene black (AB) and nickel foam were purchased from Sigma Aldrich. All chemicals were of analytical grade and used as such without any further purification.

2.2 Synthesis of CMO

Copper manganese oxide, $\text{Cu}_{1.5}\text{Mn}_{1.5}\text{O}_4$ (CMO), spinel nanocrystal was prepared by simple chemical co-precipitation method [43]. Copper acetate (0.05 M) and manganese acetate (0.1 M) were dissolved in deionized water (50 ml) and stirred for 15 min. The mixed solution was added to sodium hydroxide (0.05 M) dissolved in 50 ml deionised water under vigorous stirring at 25°C. After 10 min, the pH of the solution was adjusted to 11 by adding alkali solution. Further, the solution was stirred for 30 min in hot condition. The obtained precipitate was filtered, washed with water several times and once with ethanol to remove any other impurities present. It was dried in air for 24 h and calcinated at 300°C for 3 h to get the purified CMO. Figure 1 represents the schematic diagram for the synthesis of CMO.

2.3 Characterization

FTIR spectra of the prepared CMO was recorded using Perkin-Elmer Spectrometer over the wavelength range of $400\text{--}4000\text{ cm}^{-1}$ using KBr as a reference to determine the functional group. The phase formation, crystalline structure

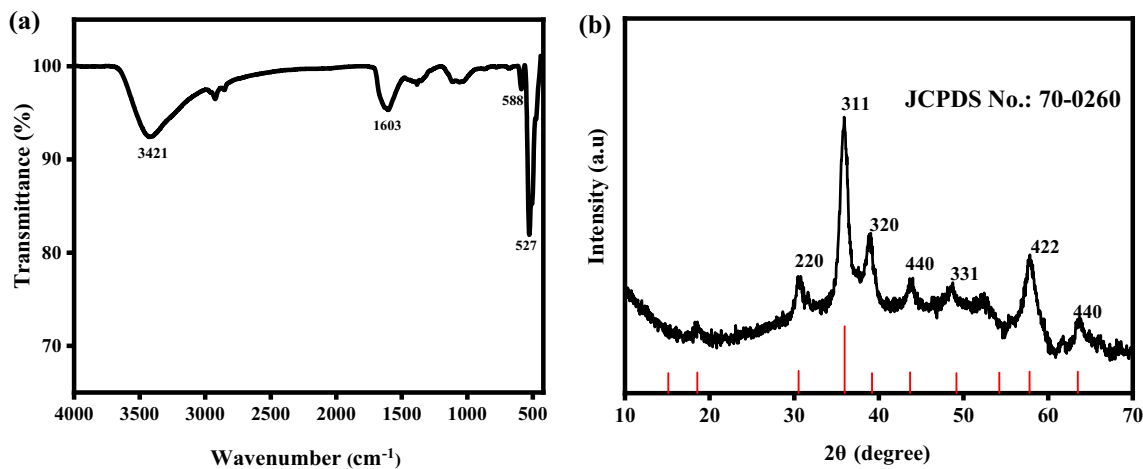


Figure 3. (a) FTIR spectra and (b) XRD pattern and its corresponding JCPDS pattern of CMO.

and particle size were investigated by X-ray powder diffraction (X'pert PRO analytical diffractometer) using Cu K_{α} as radiation ($\alpha = 1.5418 \text{ \AA}$) as X-ray source. The composition of the element and oxidation states were analysed using X-ray photoelectron spectroscopy (XPS) with Thermo Scientific MULTILAB 2000 using Al K_{α} as a radiation source. Surface morphology and elemental composition were analysed by SEM with energy-dispersive X-ray spectroscopy (EDAX) using TESCAN (Bruker) microscope. The microstructure was observed by TEM using FEI Tecnai 20 G2 microscope. The electrochemical performance was analysed by Biologic (SP-120) workstation.

2.4 Electrode preparation and electrochemical characterization

The active material was mixed with acetylene black (AB, conducting material) and polyvinylidene difluoride (PVDF, binder) in the ratio 80:15:5. The mixture was continuously ground in a mortar and the required amount of *N*-methyl-2-pyrrolidone (NMP) was used as solvent to make a

homogenous slurry. Nickel foam was pretreated and washed in acetone, HCl, distilled water and anhydrous ethanol. After washing, it was dried in hot air oven at 80°C for 12 h. The homogenous slurry was coated on nickel foam, which acts as a current collector and then it was dried at 80°C for 12 h in an oven. After drying, it was uniaxially pressed. The weight of the coated material ($\sim 4 \text{ mg}$) was maintained by measuring the weight of the Ni foam before and after coating [44]. The percentage composition and the mixing procedure for the different electrode materials are given in table 1. The active material was mixed with AB, PVDF, NMP as mentioned in table 1. The prepared electrode is shown in figure 2.

The standard three-electrode cell configuration was used for electrochemical studies. The active material coated on nickel foam performs as working electrode, Ag/AgCl (3 M KCl) and Pt wire acts as reference and counter electrode, respectively. The electrolyte used was 5 M potassium hydroxide. The CV and GCD studies were carried out in the potential range between 0 and 0.5 V with different scan rates ranging from 5 to 50 mV s^{-1} and different current densities from 1 to 5 A g^{-1} , respectively. EIS was also studied by applying an alternate current (AC) in the

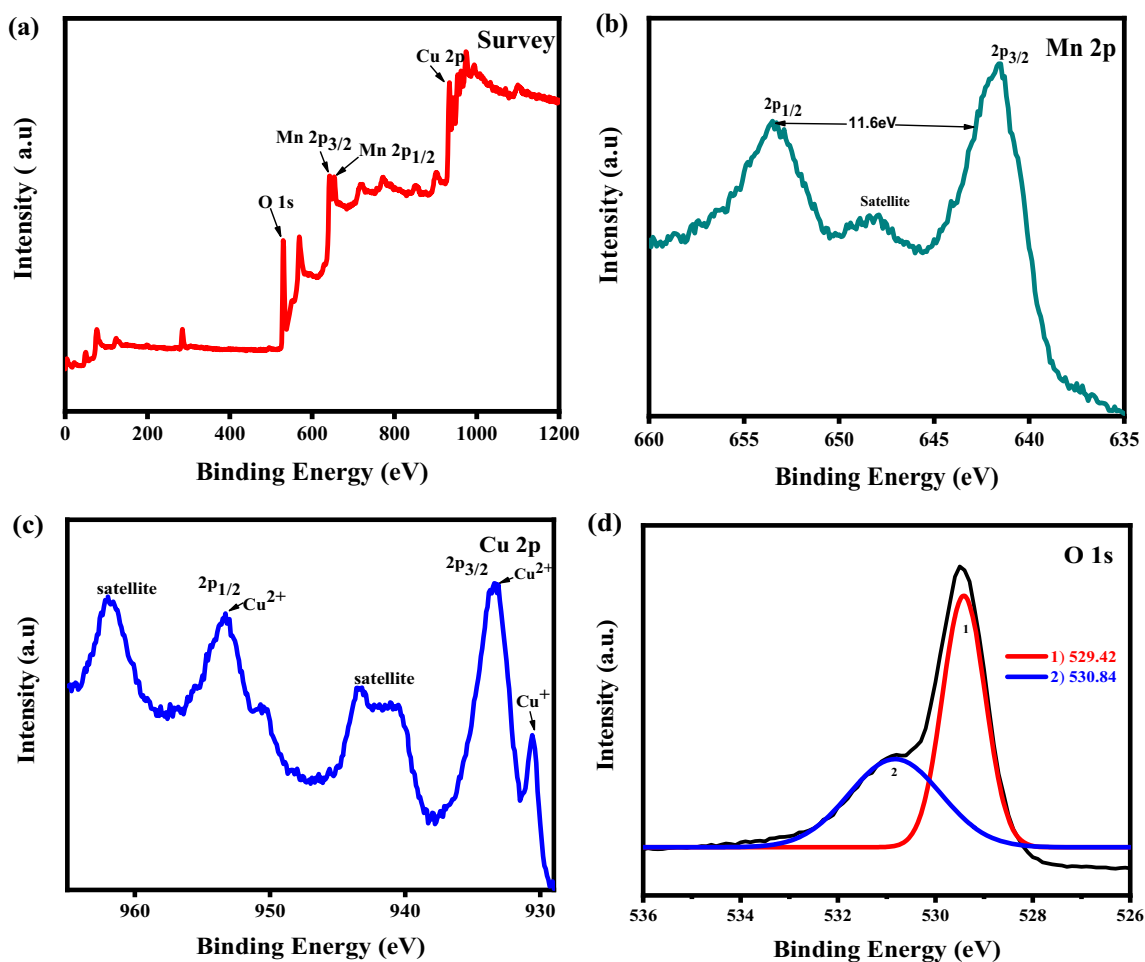


Figure 4. XPS spectra of CMO: (a) survey spectrum, (b) Mn 2p, (c) Cu 2p and (d) deconvoluted O 1s.

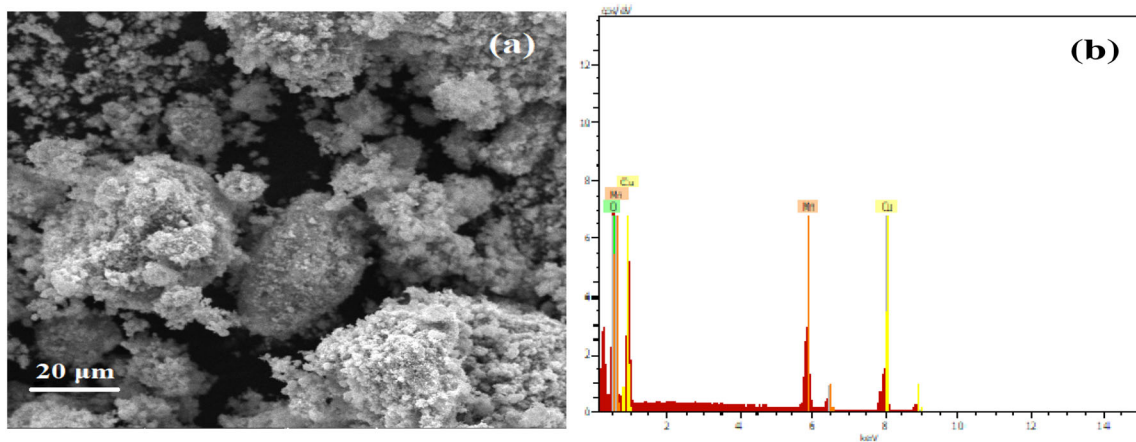


Figure 5. (a) SEM image and (b) EDAX spectrum of CMO.

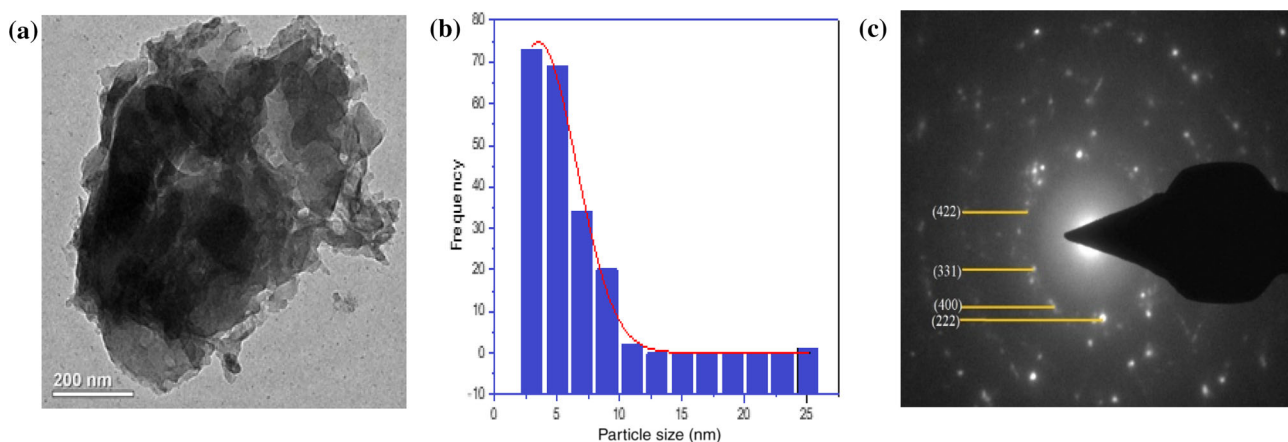


Figure 6. (a) TEM images, (b) histogram and (c) selected area electron diffraction spectrum of CMO.

frequency range from 100 kHz to 10 mHz. The specific capacitance of the electrode material from the discharge curve was calculated by using equation (1) [45]

$$C = I\Delta t/m\Delta V, \tag{1}$$

where C is the specific capacitance of the electrode material ($F\ g^{-1}$), I the applied current for charge–discharge cycles (A), Δt the discharge time (s), m the mass of the working electrode (g) and ΔV the operating potential window (V). The columbic efficiency can be calculated by the following equation (2)

$$\eta = [\Delta t_{\text{discharge}}/\Delta t_{\text{charge}}] \times 100\%, \tag{2}$$

where, η is the columbic efficiency, $t_{\text{discharge}}$ the discharging time and t_{charge} the charging time.

3. Results and discussions

3.1 FTIR spectroscopy

FTIR was accomplished to detect the functional groups of the CMO and is depicted in figure 3a. FTIR spectra in the

region $400\text{--}700\ \text{cm}^{-1}$ is related to the spinel structure. The sharp peak at $527\ \text{cm}^{-1}$ corresponds to the stretching bond of Cu–O in the tetrahedral site. The band that appeared at $588\ \text{cm}^{-1}$ associates with the stretching bond of Mn–O in octahedral site [46]. This agrees the formation of spinel $\text{Cu}_{1.5}\text{Mn}_{1.5}\text{O}_4$. The broad band detected at $3421\ \text{cm}^{-1}$ and a small band at $1603\ \text{cm}^{-1}$ provide the stretching and bending vibrations of –OH group, arising due to the adsorption of water on the nanocrystal surface [47]. The stretching frequencies obtained in the FTIR spectra confirm the formation of CMO.

3.2 XRD analysis

The XRD pattern of the CMO was recorded and depicted in figure 3b. The peaks observed at the 2θ values are 30.86° , 35.86° , 38.92° , 43.60° , 48.42° , 53.02° , 57.74° and 63.51° which correspond to the lattice planes (220), (311), (222), (400), (331), (422), (511) and (440), respectively. The diffraction peaks were matched with the standard reference JCPDS card no.70-0260. The CMO prepared by the simple co-precipitation method exhibits the cubic $\text{Cu}_{1.5}\text{Mn}_{1.5}\text{O}_4$

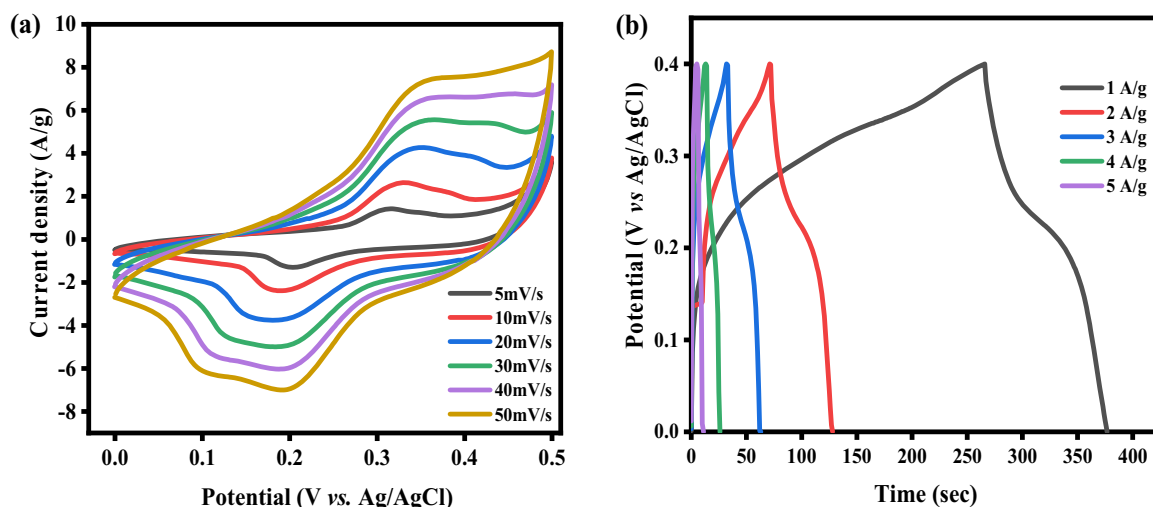


Figure 7. (a) CV and (b) GCD curve of CMO at various scan rates and current densities.

(P4332 space group) with the lattice constant $a = b = c = 8.2800$ Å. The obtained diffraction pattern confirms the formation of CMO nanocrystal. No additional peaks appeared, indicating the high purity of the electrode material. The CMO belongs to inverse cubic spinel structure, where manganese ions are distributed among the tetrahedral and octahedral sites, while copper ions are located at the octahedral sites [48]. The average crystallite size was calculated from the high intensity peak using the Debye–Scherrer equation (3) [49]

$$D = K\lambda/\beta\cos\theta, \quad (3)$$

where D (nm) is the crystalline size, K the diffraction constant (~ 0.9), λ the wavelength of the incident X-ray, β the full-width half-maximum multiplies and θ the angle of diffraction. The average crystallite size was found to be 1.38 nm using equation (3)

3.3 XPS analysis

Further the oxidation state with the elemental composition of the prepared CMO was analysed using XPS and is shown in figure 4a. XPS spectrum of Mn2p depicted in figure 4b shows two peaks at 641.6 and 653.45 eV, which are attributed to Mn2p_{3/2} and Mn2p_{1/2} levels, respectively. The spin energy separation of 11.6 eV is smaller than 11.7 eV of standard manganese oxide [50]. This confirms the doping of Cu in manganese oxide [51, 52]. The binding energy of Mn2p_{3/2} peaks at 641.6 eV shows the existence of Mn³⁺ [53, 54] and the satellite peak at 647.26–649.51 eV belongs to MnO satellite feature [55]. XPS spectrum of Cu 2p level is presented in figure 4c. The broad peak at 933.3 eV corresponds to Cu²⁺ and 930.73 eV corresponds to Cu⁺ [56].

The satellite peak at 941 and 943 eV belongs to Cu²⁺ contribution [56, 57] (Cu⁺ is diamagnetic and, consequently, does not show shake-up satellite structure). The peak at 953 eV indicates the presence of Cu in Cu²⁺ state [58]. The existence of redox equilibrium between Cu and Mn as $\text{Cu}^+ + \text{Mn}^{4+} \leftrightarrow \text{Mn}^{3+} + \text{Cu}^{2+}$ exists in Cu_{1.5}Mn_{1.5}O₄ phase [59, 60]. Figure 4d shows the deconvoluted XPS spectrum of O1s. The two peaks located at 529.42 and 530.84 eV confirm that the oxygen in this sample is present in the form of oxide [61, 62].

3.4 Morphological analysis

The surface morphology and the composition of the CMO were analysed by SEM with EDAX analysis. Spherical-like nanocrystals are observed for CMO (figure 5a). The presence of predominant characteristic elemental peak in the EDAX spectra, namely copper, manganese and oxygen, are shown in figure 5b and confirmed the prepared CMO is in pure form.

The magnified surface morphology of the prepared CMO was further confirmed by TEM image and is shown in figure 6a. The average particle size was analysed quantitatively by fitting the histogram and ImageJ software (figure 6b) and is found to be the order of 3.51 nm. The grain size observed by the TEM is closer to the crystallite size obtained from the XRD pattern, confirming the formation of monocrystalline particles and the grain sizes of which are close to the values revealed by a study on similar spinel materials [63]. The selected area electron diffraction pattern shown in figure 6c indicates the presence of (222), (400), (331) and (422) planes, which are in good agreement with XRD pattern of the prepared CMO.

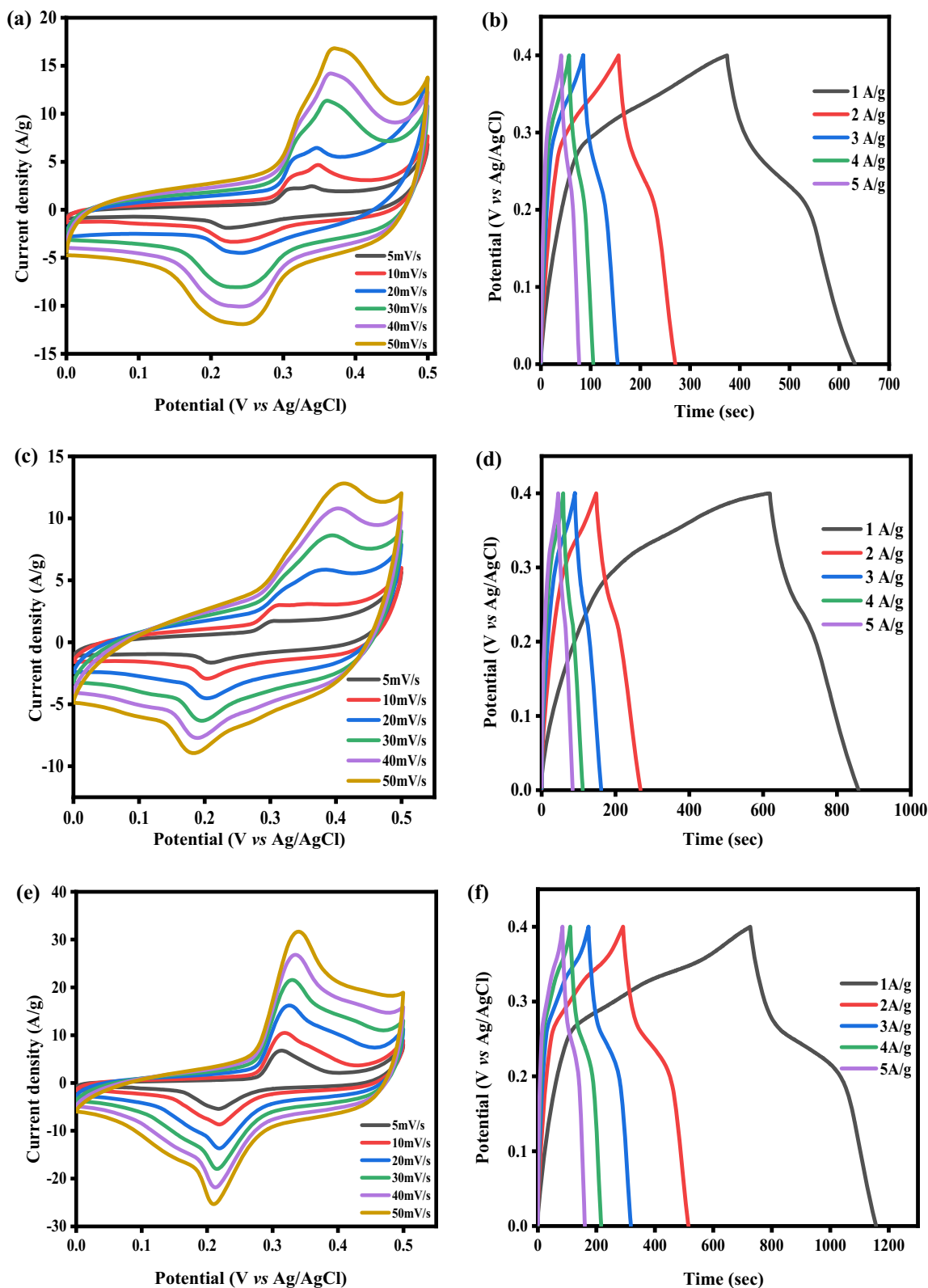
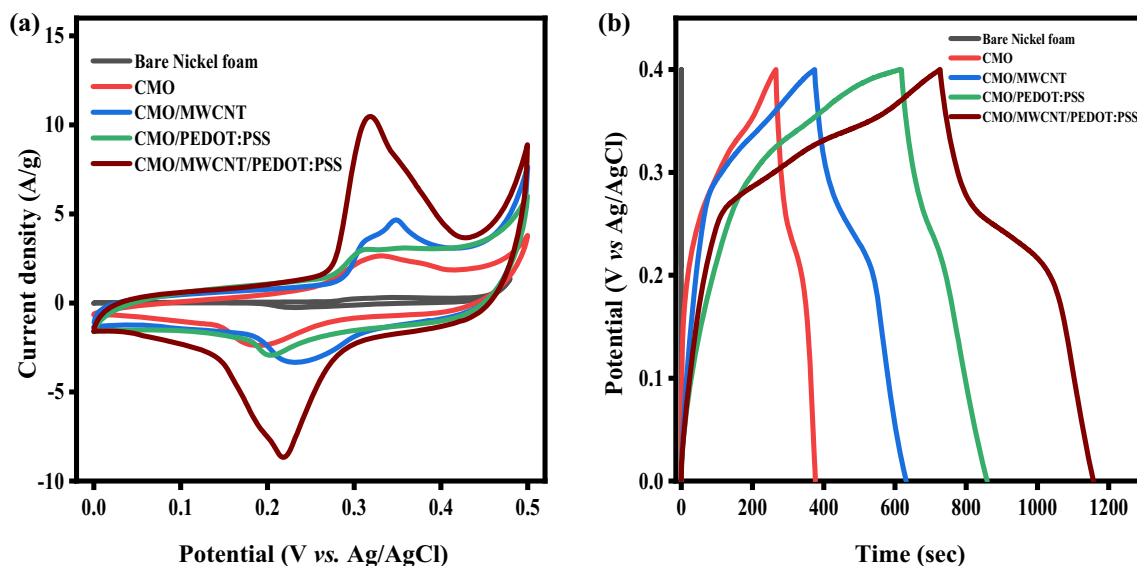


Figure 8. (a, b) CV and GCD curves of CMO/MWCNT, (c, d) CMO/PEDOT:PSS, (e, f) CMO/MWCNT/PEDOT:PSS at different scan rates and current densities.

Table 2. Specific capacitance value with current density of the electrode materials.

Current density ($A\ g^{-1}$)	Specific capacitance ($F\ g^{-1}$)			
	CMO	CMO/MWCNT	CMO/PEDOT:PSS	CMO/MWCNT/PEDOT:PSS
1	280	645	604	1087
2	250	569	580	1061
3	186	525	521	1048
4	107	486	511	1007
5	70	458	493	937

**Figure 9.** (a) CV and (b) GCD curve of bare Nickel foam, CMO, CMO/MWCNT, CMO/PEDOT:PSS, CMO/MWCNT/PEDOT:PSS at scan rate of $10\ mV\ s^{-1}$ and current density of $1\ A\ g^{-1}$.

4. Electrochemical characterizations

4.1 Effect of MWCNT, PEDOT:PSS doping on the electrochemical performance of CMO electrode material

Figure 7a displays the CV curve of CMO at various scan rates. It is clearly seen from the graph that the CMO exhibits pseudocapacitance behaviour, as it has the redox peak with the potential window of 0 to 0.5 V. The redox peak may be due to the conversion of Cu^{2+}/Cu^{+} and Mn^{4+}/Mn^{3+} . The area under the CV curve increases with increase in the scan rate. This may be due to the diffusion rate of electrolyte ions. Even at high scan rate of $50\ mV\ s^{-1}$, the materials retain their shape in the CV curve indicating the good electrical conductivity of the electrode materials. Figure 7b depicts the GCD curve of CMO. The specific capacitance of the GCD curve was calculated using equation (1). The calculated specific capacitances of CMO are 280, 250, 186, 107, 70 $F\ g^{-1}$ at current densities of 1, 2, 3, 4, 5 $A\ g^{-1}$. The above results indicate that the specific capacitance decreases with increase in current density. This

may be due to the diffusion of ions at different current rates. At a lower current density, the electrolyte ions have enough time to enter into the inner pores of the electrode surface to attain the maximum utilization of the active surface areas of the electrode materials [64, 65], whereas at high current densities, only the surface of the electrode materials is accessed by the electrolyte ions. The electrolyte ions could not find sufficient time to intercalate the inner pores of the electrode surfaces to obtain the maximum utilization of the active surface areas of the electrode materials.

Figure 8 shows the individual CV and GCD curves of CMO/MWCNT, CMO/PEDOT:PSS and CMO/MWCNT/PEDOT:PSS at different scan rates and current densities. The calculated specific capacitances of the electrode materials are given in table 2. The increase in specific capacitance value can be clearly seen from CMO to CMO/MWCNT/PEDOT:PSS electrode material. This may be due to the addition of minimum amount of dopant to the CMO, which increases the electroactivity of the electrode. The specific capacitance of the CMO/MWCNT and

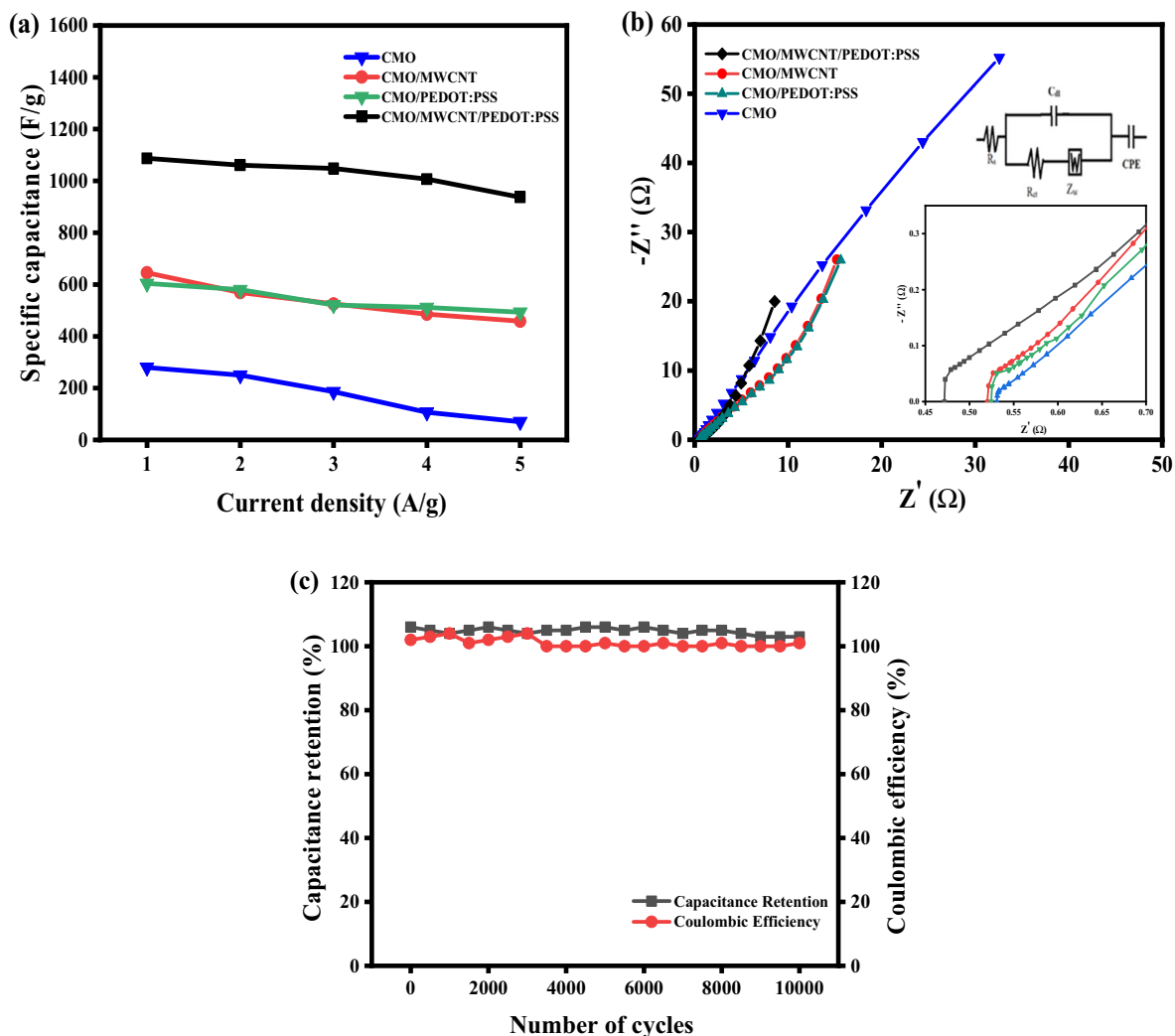


Figure 10. (a) Specific capacitance as a function of current density for CMO, CMO/MWCNT, CMO/PEDOT:PSS and CMO/MWCNT/PEDOT:PSS electrode materials. (b) Nyquist plot for CMO, CMO/MWCNT, CMO/PEDOT:PSS and CMO/MWCNT/PEDOT:PSS electrodes (insets are the magnified view of Nyquist plots at high frequency region and the equivalent circuit). (c) Cyclic stability of CMO/MWCNT/PEDOT:PSS for 10,000 cycles at 5 A g⁻¹.

Table 3. Parameters obtained by fitting of the experimental impedance data, calculated specific capacitance and electrochemical surface area (ECSA).

Electrode	R_s (Ω)	R_{ct} (Ω)	C (mF)	CPE (mF)	W (Ω)	C_{dm} (mF)	ECSA (m ² g ⁻¹)
CMO	0.530	0.0118	2.19	187	0.061	111.9	559
CMO/MWCNT	0.520	0.0105	2.62	376	0.127	251.50	1257
CMO/PEDOT:PSS	0.524	0.0115	2.51	354	0.119	241.28	1206
CMO/MWCNT/PEDOT:PSS	0.471	0.0108	11.18	620	0.712	308.84	1544

CMO/PEDOT:PSS are nearly equal, but doping of both MWCNT and PEDOT:PSS on CMO (CMO/MWCNT/PEDOT:PSS) shows the highest specific capacitance value.

Figure 9a and b shows the CV and GCD curves of bare nickel foam, CMO, CMO/MWCNT, CMO/PEDOT:PSS,

CMO/MWCNT/PEDOT:PSS electrodes at a scan rate of 10 mV s⁻¹ and at a current density of 1 A g⁻¹, respectively. It shows the influence of MWCNT, PEDOT and the nature of dopants on the electrochemical behaviour of CMO electrode. The CV curve exhibits the redox behaviour

Table 4. Comparative table of specific capacitance and cycling stability of various metal oxide-based materials in different electrolytes.

Electrode material	Electrolyte	Specific capacitance	Cycling stability	Refs.
Mn ₃ O ₄	1 M Na ₂ SO ₄	322 F g ⁻¹ at 0.5 mA cm ⁻²	77% over 1000cycles	[69]
Mn ₃ O ₄ NPs/AC	2 M TEABF ₄	216 F g ⁻¹ at 0.5 A g ⁻¹	85% over 500cycles	[26]
Co-doped MnO	2 M KCl	186.2 F g ⁻¹ at 10 mV s ⁻¹	84% over 500 cycles	[70]
Fe-doped MnO	2 M KCl	298.4 F g ⁻¹ at 10 mV s ⁻¹	83% over 500 cycles	[70]
Manganese oxide/CNT	1 M Na ₂ SO ₄	568 F g ⁻¹ at 1 mA cm ⁻²	88% over 2500 cycles	[71]
MnO ₂ /PEDOT	1 M LiClO ₄ in acetonitrile	315 F g ⁻¹ at 1 mA cm ⁻²	85% over 500 cycles	[72]
Graphite/PEDOT/MnO ₂	0.5 M Na ₂ SO ₄	195.7 F g ⁻¹ at 0.5 A g ⁻¹	81.1% over 2000 cycles	[73]
CuO	6 M KOH	137 F g ⁻¹ at 5 mA cm ⁻²	88% over 500 cycles	[28]
CuO NPs/MWCNT	0.5 M Na ₂ SO ₄	452.85 F g ⁻¹ at 10 mV s ⁻¹	90% over 500cycles	[74]
PEDOT/CuO	0.5 M H ₂ SO ₄	198.89 F g ⁻¹ at 5 mV s ⁻¹	68.55% over 500 cycles	[75]
CuMn ₂ O ₄	6 M KOH	571.6 F g ⁻¹ at 1 A g ⁻¹	98%	[40]
CuMn ₂ O ₄	0.1 M Na ₂ SO ₄	744 F g ⁻¹ at 10 mV s ⁻¹	91% over 10000 cycles	[41]
CuO@MnO ₂	1 M Na ₂ SO ₄	343.9 F g ⁻¹ at 0.25 A g ⁻¹	83.1% over 12,000 cycles	[39]
Cu _{1.5} Mn _{1.5} O ₄ /MWCNT/PEDOT	5 M KOH	1087 F g ⁻¹ at 1 A g ⁻¹	104% over 10,000 cycles	This study

proving the presence of faradaic charge storage mechanism. CMO/MWCNT/PEDOT:PSS shows better performance and high electrochemical activity compared to all other composites electrode. Nickel foam shows negligible electrochemical activity.

In addition, the non-linear charge/discharge curve confirms the faradaic nature of the electrode material. Further, the CMO/MWCNT/PEDOT:PSS has a higher discharge time, thereby shows higher specific capacitance compared to CMO at a current density of 1 A g⁻¹. The calculated specific capacitance of CMO/MWCNT/PEDOT:PSS at a current density of 1 A g⁻¹ is 1087 F g⁻¹, which is significantly higher than the CMO of 280 F g⁻¹ at 1 A g⁻¹. The specific capacitance of all the electrode materials as a function of different current densities is displayed in figure 10a. This demonstrates that the doping enhances the specific capacitance of CMO for the supercapacitor application.

4.2 EIS analysis

The impedance spectra was recorded for the four electrodes (CMO, CMO/MWCNT, CMO/PEDOT:PSS and CMO/MWCNT/PEDOT:PSS) and presented as Nyquist plot in figure 10b. At low frequency region, a vertical line along the y-axis more than 45° is observed. This indicates the ideal capacitive behaviour of the electrode. The equivalent circuit model which fits for all the electrodes is shown as an inset (top) in figure 10b and the parameters are tabulated in table 3. The solution resistance (R_s) of the CMO, CMO/MWCNT, CMO/PEDOT:PSS and CMO/MWCNT/PEDOT:PSS electrode obtained from the Nyquist plot is 0.530 Ω, 0.520 Ω, 0.524 Ω and 0.471 Ω, respectively. It is observed that CMO/MWCNT/PEDOT:PSS electrode has low R_s value compared to other electrode materials.

The specific capacitance, C_{dm} , can be calculated from the low frequency value of Nyquist plot using equation (4) [66, 67]

$$C_{dm} = -1/2\pi f Z'' m, \quad (4)$$

where C_{dm} is specific capacitance, Z'' is imaginary part of the impedance, f the subsequent frequency and m the mass of the electrode material. The C_{dm} value is used to calculate the electrochemical surface area (ECSA) by using equation (5) [67, 68]

$$ECSA = C_{dm}/C_d, \quad (5)$$

where C_{dm} is specific capacitance obtained from Nyquist plot and C_d a constant value of 20 μF cm⁻². The calculated values of C_{dm} and ECSA are tabulated in table 3. The calculated ECSA values are in good agreement with the specific capacitance values. CMO/MWCNT/PEDOT:PSS shows the highest ECSA, which provides the highest specific capacitance value among all the electrodes. It may be due to the pore structure of MWCNT together with the large electroactive conducting polymer and pseudocapacitive nature of CMO. CMO/MWCNT/PEDOT:PSS shows the most capacitive behaviour when compared to all the other electrodes.

4.3 Electrochemical stability

Further, to check the electrochemical stability of the electrode materials, GCD was performed for 10,000 cycles at current density of 5 A g⁻¹. Figure 10c shows the cyclic stability of CMO/MWCNT/PEDOT:PSS for 10,000 cycles at 5 A g⁻¹. It can be noticed that 104% of initial capacitance retention was retained with high coulombic efficiency of 101% over 10,000 cycles. This indicates the high stability of the CMO/MWCNT/PEDOT:PSS electrode. To

compare our results with reported values, a comparative table is provided in table 4 with specific capacitance and cycle life of several metal oxide-based electrodes in different electrolytes.

5. Conclusions

This work involves the synthesis of spinel CMO nanocrystals by a simple chemical co-precipitation method. XRD pattern reveals the formation of cubic with inverse spinel structure. SEM and TEM analyses show the crystallite particle size to be 3.51 nm, and the elemental composition confirms the presence of Cu, Mn and O. Further, the oxidation state and elemental composition was analysed by XPS and confirms the presence of $\text{Cu}_{1.5}\text{Mn}_{1.5}\text{O}_4$ nanocrystals. The electrochemical performance of CMO shows a specific capacitance of 280 F g^{-1} at the current density of 5 A g^{-1} . To enhance its electrochemical performance, it was doped with MWCNT and PEDOT:PSS. The specific capacitance values of CMO/MWCNT and CMO/PEDOT:PSS are 645 and 604 F g^{-1} at the current density of 1 A g^{-1} , respectively. CMO/MWCNT/PEDOT:PSS electrode shows a very high specific capacitance value of 1087 F g^{-1} at a current density of 1 A g^{-1} , with good rate performance retained with an excellent electrochemical stability of 104% capacitance retention, having coulombic efficiency of 101% over 10,000 cycles at a current density of 5 A g^{-1} . This study shows the excellent performance of CMO/MWCNT/PEDOT:PSS suitable for supercapacitor applications.

References

- [1] Burke A 2000 *J. Power Sources* **91** 37
- [2] Zhao X, Sánchez B M, Dobson P J and Grant P S 2011 *Nanoscale* **3** 839
- [3] Zhang L L and Zhao X S 2009 *Chem. Soc. Rev.* **38** 2520
- [4] Wang G, Zhang L and Zhang J 2012 *Chem. Soc. Rev.* **41** 797
- [5] Bose S, Kuila T, Mishra A K, Rajasekar R, Kim N H and Lee J H 2012 *J. Mater. Chem.* **22** 767
- [6] El-Kady M F, Strong V, Dubin S and Kaner R B 2012 *Science* **335** 1326
- [7] Pan H, Li J Y and Feng Y P 2010 *Nanoscale Res. Lett.* **5** 654
- [8] Tang W, Liu L, Tian S, Li L, Yue Y, Wu Y *et al* 2011 *Chem. Commun.* **47** 10058
- [9] Yan J, Fan Z, Sun W, Ning G, Wei T, Zhang Q *et al* 2012 *Adv. Funct. Mater.* **22** 2632
- [10] Hu H, Guan B Y and David Lou X W 2016 *Chem.* **1** 102
- [11] Eftekhari A, Li L and Yang Y 2017 *J. Power Sources* **347** 86
- [12] Lei C, Wilson P and Lekakou C 2011 *J. Power Sources* **196** 7823
- [13] Huang Y, Tao J, Meng W, Zhu M, Huang Y, Fu Y *et al* 2015 *Nano Energy* **11** 518
- [14] Min L, Ahmed A, Pascal R, Sabine S and Rabah B 2020 *J. Colloid Interface Sci.* **579** 520
- [15] Mohapatra S, Acharya A and Roy G S 2012 *Lat. Am. J. Phys. Educ.* **6** 380
- [16] Xu J and Wang L 2019 *Sci. Rep.* **9** 12557
- [17] Wu J, Mi R, Li S, Guo P, Mei J, Liu H *et al* 2015 *RSC Adv.* **5** 25304
- [18] Vignesh V, Subramani K, Sathish M and Navamathava R 2018 *Colloid Surf. A* **538** 668
- [19] Yang T, Xia D, Wang Z and Chen Y 2009 *Mater. Lett.* **63** 5
- [20] Lavela P, Tirado J L and Vidal-ABarca C 2007 *Electrochim. Acta* **52** 7986
- [21] Sharma Y, Sharma N, Subba Rao G V and Chowdari B V R 2007 *J. Power Sources* **173** 495
- [22] Lavela P and Tirado J L 2007 *J. Power Sources* **172** 379
- [23] Bomio M, Lavela P and Tirado J L 2008 *J. Solid State Electrochem.* **12** 729
- [24] Zhou L, Zhao D and Lou X W 2012 *Adv. Mater.* **24** 745
- [25] Saravanakumar B, Radhakrishnan C, Ramasamy M, Kalia-perumal R, Britten A J and Mkandawire M 2019 *Results Phys.* **13** 102185
- [26] Bui P T M, Song J, Li Z, Akhtar M S and Yang O 2017 *J. Alloys Compd.* **694** 560
- [27] Kang J, Chen L, Hou Y, Li C, Fujita T, Lang X *et al* 2013 *Adv. Energy Mater.* **3** 857
- [28] Zhang Y X, Huang M, Kuang M, Liu C P, Tan J L and Dong M 2013 *Int. J. Electrochem. Sci.* **8** 1366
- [29] Chen S, Tang W, He J, Miao R and Lin H 2018 *J. Mater. Chem. A* **6** 9047
- [30] Batoo K M and Abd El-sadek M S 2013 *J. Alloys Compd.* **566** 112
- [31] Hilczer A, Kowalska K, Markiewicz E, Pietraszko A and Andrzejewski B 2016 *Mater. Sci. Eng. B* **207** 47
- [32] Albuquerque A S, Tolentino M V C, Ardisson J D, Moura F C C, de Mendonça R and Macedo W A A 2012 *Ceram. Int.* **38** 2225
- [33] Wright P A, Natarajan S, Thomas J M and Gai-Boyes P L 1992 *Chem. Mater.* **4** 1053
- [34] Ali R, Mahmood A, Khan M A, Chughtai A H, Shahid M, Shakir I *et al* 2014 *J. Alloys Compd.* **584** 363
- [35] Priyadharsini P, Pradeep A, Rao P S and Chandrasekaran G 2009 *Mater. Chem. Phys.* **116** 207
- [36] Yang H, Zhang X, Ao W and Qiu G 2004 *Mater. Res. Bull.* **39** 833
- [37] Shoemaker D P, Li J and Seshadri R 2009 *J. Am. Chem. Soc.* **131** 11450
- [38] Ranjbar-Nouri Z, Soltanieh M and Rastegari S 2018 *Surf. Coat. Technol.* **334** 365
- [39] Chen H, Zhou M, Wang T, Li F and Zhang Y X 2016 *J. Mater. Chem. A* **4** 10786
- [40] Saravanakumar B, Muthu Lakshmi S, Ravi G, Ganesh V, Sakunthala A and Yuvakkumar R 2017 *J. Alloys Compd.* **723** 115
- [41] Sheikhzadeh M and Sanjabi S 2021 *Synth. Met.* **278** 116802
- [42] Jingbin Q, Lin M, Zheng M, Jichun H and Decheng L 2016 *RSC Adv.* **6** 55786
- [43] Li-Na C, Yue G, An-Hui L, Branton P and Li W-C 2012 *J. Mol. Catal. A Chem.* **360** 35
- [44] Zhao X, Hou Y, Wang Y, Yang L, Zhu L, Caoc R *et al* 2017 *RSC Adv.* **7** 40286

- [45] Xiong P, Hu C, Fan Y, Zhang W, Zhu J and Wang X 2014 *J. Power Sources* **266** 384
- [46] Mendez-Martinez F, Gonzalez F, Lima E, Bosch P and Pfeiffer H 2010 *J. Mex. Chem. Soc.* **54** 2
- [47] Rahman A, Ismail A, Jumbianti D, Magdalena S and Sudrajat H 2009 *Indo. J. Chem.* **9** 355
- [48] Al-Senani G M, Abd-Elkader O H and Deraz N M 2021 *Appl. Sci.* **11** 2034
- [49] Murty B S, Shankar P, Raj Baldev, Rath B B and Murday J 2013 *Textbook of nanoscience and nanotechnology* 1st edn. (Heidelberg: Springer Berlin), co-published with Universities Press (India) Pvt. Ltd.
- [50] Audi A A and Sherwood P M A 2002 *Surf. Interface Anal.* **33** 274
- [51] Li J, Xiong S, Li X and Qian Y 2012 *J. Mater. Chem.* **22** 23254
- [52] Yang Z, Zhang W, Wang Q, Song X and Qian Y 2006 *Chem. Phys. Lett.* **418** 46
- [53] Gautier J L, Rios E, Gracia M, Marco J F and Gancedo J R 1997 *Thin Solid Films* **311** 51
- [54] Liu H Y, Zhu X F, Li M R, Tang Q W, Sun G Q and Yang W S 2014 *Electrochim. Acta* **144** 31
- [55] Sun R, Wang L, Yu H, Zain ul A, Chen Y, Khalid H *et al* 2016 *J. Inorg. Organomet. Polym.* **26** 545
- [56] Marco J F, Gancedo J R, Nguyen Cong H, del Canto M and Gautier J L 2006 *Solid State Ionics* **177** 1381
- [57] Stewart S J, Multigner M, Marco J F, Berry F J, Hernando A and Gonzalez J M 2004 *Solid State Commun.* **130** 247
- [58] Einaga H, Kiya A, Yoshioka S and Teraoka Y 2014 *Catal. Sci. Technol.* **4** 3713
- [59] Vandenberghe R, Legrand E, Scheerlinck D and Brabers V 1976 *Acta Crystallogr. Sect. B: Struct. Crystallogr. Cryst. Chem.* **32** 2796
- [60] Bayon R, Vicente G S, Maffiotte C and Morales A 2008 *Sol. Energy Mater. Sol. Cells* **92** 1211
- [61] Xie S, Liu Y, Deng J, Zhao X, Yang J, Zhang K *et al* 2016 *J. Catal.* **342** 17
- [62] Sakunthala A, Reddy M V, Selvasekarapandian S, Chowdari B V R and Selvin P C 2011 *Energy Environ. Sci.* **4** 1712
- [63] Zákutná D, Vlček J, Fitl P, Nemkovski K, Honecker D, Nižňanský D *et al* 2018 *Phys. Rev. B* **98** 064407
- [64] Heydari H, Moosavifard S E, Shahraki M and Elyasi S 2017 *J. Energy Chem.* **26** 762
- [65] Vijayakumar S, Nagamuthu S and Muralidharan G 2013 *ACS Appl. Mater. Interfaces* **5** 2188
- [66] Zhang J and Zhao X S 2012 *ChemSusChem* **5** 818
- [67] Joshi A, Sahu V, Singh G and Sharma R K 2019 *Sustain. Energy Fuels* **3** 1248
- [68] Ali G A M, Yusoff M M, Shaaban E R and Chong K F 2017 *Ceram. Int.* **43** 8440
- [69] Gnana B, Raj S, Asiri A M, Wu J J and Anandan S 2015 *J. Alloys Compd.* **636** 234
- [70] Dung Dang T, Thu Hang Le T, Bich Thuy Hoang T and Tung Mai T 2015 *Adv. Nat. Sci. Nanosci. Nanotechnol.* **6** 025011
- [71] Fan Z, Chen J, Wang M, Cui K, Zhou H and Kuang Y 2006 *Diam. Relat. Mater.* **15** 1478
- [72] Sena P, De Amitabha, Dutta Chowdhury A, Bandyopadhyaya S K, Agnihotri N and Mukherjee M 2013 *Electrochim. Acta* **108** 265
- [73] Tang P, Han L and Zhang L 2014 *ACS Appl. Mater. Interfaces* **6** 10506
- [74] Paulose R and Mohan R 2019 *J. Nanosci. Nanotechnol.* **19** 8151
- [75] Ates M, Akif Serin M, Ekmen I and Ertas Yavuz N 2015 *Polym. Bull.* **72** 2573